



# Influence of the crystalline phase and surface area of the TiO<sub>2</sub> support on the CO oxidation activity of mesoporous Au/TiO<sub>2</sub> catalysts

Y. Denkwitz<sup>a</sup>, M. Makosch<sup>a</sup>, J. Geserick<sup>b</sup>, U. Hörmann<sup>c</sup>, S. Selve<sup>c</sup>, U. Kaiser<sup>c</sup>, N. Hüsing<sup>b</sup>, R.J. Behm<sup>a,\*</sup>

<sup>a</sup> Institute of Surface Chemistry and Catalysis, Ulm University, D-89069 Ulm, Germany

<sup>b</sup> Institute of Inorganic Chemistry I, Ulm University, D-89069 Ulm, Germany

<sup>c</sup> Central Facility of Electron Microscopy, Ulm University, D-89069 Ulm, Germany

## ARTICLE INFO

### Article history:

Received 13 March 2009

Received in revised form 15 June 2009

Accepted 18 June 2009

Available online 24 June 2009

### Keywords:

Mesoporous catalysts

Activity

Deactivation

Au/TiO<sub>2</sub>

CO oxidation

## ABSTRACT

The influence of the TiO<sub>2</sub> crystalline phase and of the surface area on the activity and stability/deactivation behavior of structurally well-defined mesoporous Au/TiO<sub>2</sub> catalysts with comparable Au loading in the CO oxidation reaction was investigated by kinetic measurements under differential reaction conditions and by *in situ* DRIFTS. The crystalline phase and surface area of the TiO<sub>2</sub> substrate were controlled by the pH and the type of the structure-directing surfactants applied in the synthesis. Au loading of the mesoporous oxides was performed by the same deposition–precipitation procedure for all catalysts. The resulting trends in the CO oxidation behavior, including the TOF based activities and the stability/deactivation behavior are discussed.

© 2009 Elsevier B.V. All rights reserved.

## 1. Introduction

Oxide supported Au catalysts have been demonstrated to be highly active already at low temperatures for various oxidation and reduction reactions, most prominently the CO oxidation reaction [1–3], which in turn is of interest in environmental catalysis applications such as the preferential oxidation of CO in H<sub>2</sub> feed gases for fuel cells. It turned out, that in addition to other properties, the nature of the supporting oxide has a significant effect on the activity of the catalyst [4–7]. Recently, mesoporous oxides were introduced as alternative support materials, which may be attractive, e.g., because of their high surface area or the stabilization of the Au nanoparticles in the mesopores of the support [7–15]. For example, Au catalysts supported on mesoporous aluminosilicates showed a higher CO oxidation activity [9–11] than Au/SiO<sub>2</sub> catalysts [6,16]. Similar observations of a higher activity were reported also for the much more active mesoporous Au/TiO<sub>2</sub> catalysts [8,12–15,17], when comparing with highly active Au/TiO<sub>2</sub> catalysts based on non-porous titania [2,18–24]. Comparing different mesoporous Au catalysts, Overbury et al. found a much higher CO oxidation activity on Au/TiO<sub>2</sub> than on Au/SiO<sub>2</sub> in temperature screening measurements [7]. Furthermore, it was reported that also the crystalline phase of the (non-porous or mesoporous) TiO<sub>2</sub> support influences the CO oxidation activity [13,25–27]. Schwarz et al. found

that the activity of non-porous Au/TiO<sub>2</sub> catalysts decreased from brookite via anatase to rutile for catalysts activated by calcination at 300 °C, while after reduction at 150 °C the activities were comparable [25], and similar observations were reported by Yan et al. for mesoporous TiO<sub>2</sub> supported catalysts [26]. These authors explained this by an increasing tendency for Au particle sintering during calcination at 300 °C in the order brookite < anatase < P25 (anatase/rutile) ≈ rutile < mesoporous [25]. In contrast, for reduction at 150 °C such effects were small. Ho et al. reported that the crystalline phase of TiO<sub>2</sub> influences also the deactivation of Au/TiO<sub>2</sub> catalysts with comparable surface areas (46–54 m<sup>2</sup> g<sup>−1</sup>), which increased in the order Au/anatase (mesoporous) > Au/P25 (non-porous rutile/anatase) > Au/rutile (mesoporous) [13]. In a comparative study on the activity of porous and non-porous Au/TiO<sub>2</sub> catalysts prepared from different crystalline phases of TiO<sub>2</sub> (anatase, rutile, P25), Comotti et al. concluded that the crystalline phase has no significant influence on the catalytic properties of the unconditioned catalysts [27]. This was different when the catalysts were calcined before reaction, where the P25 based catalyst showed a significantly higher thermostability than catalysts supported on anatase or rutile. While after calcination at 250 °C, the activities are comparable with that of the unconditioned catalysts and similar for all catalysts, calcination at 350 °C leads to lower activities for the (mesoporous) rutile or (mesoporous) anatase supported catalysts, while the P25 supported catalyst retains its activity. The decay in activity, however, is not caused by Au nanoparticle sintering, since the mean particle size of ~3.0 nm was identical for 250 and 350 °C calcination and all catalysts. On the other hand, Wang et al. reported a significant higher

\* Corresponding author. Tel.: +49 731 50 254 50; fax: +49 731 50 254 52.  
E-mail address: [juergen.behm@uni-ulm.de](mailto:juergen.behm@uni-ulm.de) (R.J. Behm).

**Table 1**TiO<sub>2</sub> crystallite size, BET surface area, pore diameter, pore volume, Au loading and weight loss (TGA) of Au/TiO<sub>2</sub> catalysts based on different (mesoporous) support materials.

Catalyst	TiO <sub>2</sub> support synthesized with	pH	Crystalline phase	TiO <sub>2</sub> crystallite size (nm)	BET surface area (m <sup>2</sup> g <sup>-1</sup> )	Pore diameter (nm)	Pore volume (cm <sup>3</sup> g <sup>-1</sup> )	Au loading (wt.%)	Weight loss <500 °C (wt.%)	Weight loss <990 °C (wt.%)
Au/TiO <sub>2</sub> (P25)	–	–	Anatase/rutile	21/30	58	–	–	3.1	2.7	2.8
Au/TiO <sub>2</sub> (1)	Brij56, EGMT	2	Anatase	9.9	106	7.5–8.2	0.18	3.0	4.6	4.8
Au/TiO <sub>2</sub> (2)	Brij56, EGMT	2	Anatase	9.9	106	7.5–8.2	0.18	2.6	3.9	4.1
Au/TiO <sub>2</sub> (3)	SDS, EGMT	2	Anatase	6.6	175	4.4–6.3	0.28	2.6	8.5	9.2
Au/TiO <sub>2</sub> (4)	SDS, EGMT	~1.2	Anatase/rutile	5.6	240	3.5	0.32	4.2	11.0	11.8
Au/TiO <sub>2</sub> (5)	SDS, EGMT	0	Rutile	6.7	160	<sup>a</sup>	0.22	4.8	6.8	9.3

<sup>a</sup> Not well defined.

activity of Au catalysts based on mesoporous rutile (5% anatase) after calcination at 500 °C compared to Au/P25 [14]. Moreau et al. reported a higher activity of a non-conditioned Au/rutile catalyst (100 m<sup>2</sup> g<sup>-1</sup>) compared to a similarly treated Au/anatase catalyst (90 m<sup>2</sup> g<sup>-1</sup>) [24]. These authors also studied the influence of the surface area of the anatase support on the CO oxidation activity, and found that the activity decreases with increasing surface area in the order 37 m<sup>2</sup> g<sup>-1</sup> > 45 m<sup>2</sup> g<sup>-1</sup> > 90 m<sup>2</sup> g<sup>-1</sup> > 240 m<sup>2</sup> g<sup>-1</sup> > 305 m<sup>2</sup> g<sup>-1</sup>. Comparable observations of a decreasing activity with increasing BET surface area were reported also by Zhu et al. for mesoporous Au/TiO<sub>2</sub> catalysts, comparing a 55 m<sup>2</sup> g<sup>-1</sup> catalyst and a 141 m<sup>2</sup> g<sup>-1</sup> catalyst [15]. Summarizing these results, the activity and stability of mesoporous Au/TiO<sub>2</sub> catalysts seem to be affected by various properties, including (i) the size of the oxide crystallites and Au nanoparticles and the respective surface areas, (ii) the structure and size of the oxide pores, and (iii) the crystalline phase of the TiO<sub>2</sub> support (anatase/rutile). Clear trends, however, can hardly be extracted from these data because of the wide variations in parameters.

For a more detailed understanding, we started a systematic study on the CO oxidation behavior of Au catalysts based on mesoporous TiO<sub>2</sub> whose structural properties were systematically varied. Recently we reported that mesoporous Au/TiO<sub>2</sub> catalysts prepared by sol–gel processing and subsequent Au deposition on the mesoporous TiO<sub>2</sub> via a deposition–precipitation procedure show a higher CO oxidation activity than catalysts prepared in a similar way from a commercially available (P25, Degussa) non-porous support, with a comparable Au particle size and Au metal loading [12]. In the present paper, we report on the influence of the TiO<sub>2</sub> crystalline phase of mesoporous Au/TiO<sub>2</sub> catalysts on their CO oxidation activity and deactivation behavior. Mesoporous TiO<sub>2</sub> materials with high surface areas and of different crystalline phases were synthesized via sol–gel processing as described in Ref. [28]. For comparison, we also include a standard Au/TiO<sub>2</sub> catalyst based on a P25 support. The structure and surface composition of the catalysts were characterized by X-ray diffraction (XRD), transmission electron microscopy (TEM), X-ray photoelectron spectroscopy (XPS) and temperature programmed desorption (TPD) (Section 3.1). Stimulated by our recent finding of a pronounced effect of a catalyst drying step prior to catalyst

conditioning on the CO oxidation behavior of P25 supported Au/TiO<sub>2</sub> catalysts [29], we also evaluated the influence of a similar catalyst pre-treatment on the reaction behavior (Section 3.2). The activities as well as the deactivation and re-activation behavior during CO oxidation were evaluated by kinetic measurements under differential reaction conditions (Section 3.3). Mechanistic information was obtained from *in situ* IR measurements performed under similar reaction conditions, employing diffuse reflectance IR spectroscopy (DRIFTS).

## 2. Experimental set-up and procedures

### 2.1. Preparation of the mesoporous TiO<sub>2</sub> support and the Au catalysts

The mesoporous TiO<sub>2</sub> support material was prepared via an ethylene glycol-modified titanium precursor (bis(2-hydroxyethyl)titanate, EGMT) [28]. EGMT was synthesized by modifying a procedure described by Xia et al. [30]. For the catalysts (1) and (2), the mesoporous TiO<sub>2</sub> support was synthesized by dissolving polyethylene oxide hexadecylether (Brij56) in dilute hydrochloric acid (pH 2). Subsequently, EGMT was added, and the solution was ultrasonicated for 5 h at 60 °C. The resulting suspension was aged at 60 °C for 24 h, and then centrifuged. The precipitate was washed with water three times and subsequently calcined at 400 °C for 4 h. The mesoporous support for the catalysts (3)–(5) was synthesized with sodium dodecyl sulfate (SDS) and EGMT to obtain higher surface areas. The different polymorphs of titania (anatase and rutile) were accessible by variation of the pH-value (see Table 1).

The Au/TiO<sub>2</sub> catalysts were prepared via a deposition–precipitation procedure described in [23,31]. In short, TiO<sub>2</sub> was suspended in water at 60 °C at a pH of 5–5.5, followed by addition of tetrachloroauric acid (HAuCl<sub>4</sub>·4H<sub>2</sub>O). A constant pH value was maintained by addition of Na<sub>2</sub>CO<sub>3</sub> solution. After additional 30 min of stirring, the precipitate was cooled to room temperature, filtered, washed and dried overnight at room temperature under vacuum. The catalysts were stored in the dark at –10 °C. The Au metal loading (Table 2) was determined by inductively coupled plasma atom emission spectroscopy (ICP–AES). If not mentioned otherwise, the raw catalysts were dried in 20 N ml min<sup>-1</sup> N<sub>2</sub> at 100 °C for 15 h, then calcined (10% O<sub>2</sub> in N<sub>2</sub>) at 400 °C for 30 min,

**Table 2**Mean Au particle size, Au(4f):Ti(2p) intensity ratio, absolute and relative activity for CO oxidation of various Au/TiO<sub>2</sub> catalysts after drying in N<sub>2</sub> at 100 °C (15 h) plus calcination in 10% O<sub>2</sub>/N<sub>2</sub> at 400 °C (30 min) (N15–O400) and after re-calcination in 10% O<sub>2</sub>/N<sub>2</sub> at 400 °C (30 min).

Catalyst	Au loading (wt.%)	Au-particle size (nm)	Au(4f):Ti(2p) ratio	Initial/final activity (×10 <sup>-4</sup> mol s <sup>-1</sup> g <sub>Au</sub> <sup>-1</sup> )	Initial/final TOF (s <sup>-1</sup> )	Activity after 1000 min reaction (%)	Initial activity after re-calcination (%)
Au/TiO <sub>2</sub> (P25)	3.1	2.9 ± 0.8	0.13	34.3/9.4	2.0/0.5	28	n.m.
Au/TiO <sub>2</sub> (1)	3.0	4.1 ± 0.8	0.05	84.1/27.9	6.4/2.1	33	n.m.
Au/TiO <sub>2</sub> (2)	2.6	3.7 ± 0.9	0.04	87.1/25.7	6.3/1.9	30	n.m.
Au/TiO <sub>2</sub> (3)	2.6	3.0 ± 0.7	0.04	37.2/12.4	2.2/0.7	33	94
Au/TiO <sub>2</sub> (4)	4.2	6.1 ± 1.3	0.04	33.9/6.0	4.0/0.7	18	82
Au/TiO <sub>2</sub> (5)	4.8	6.1 ± 1.5	0.03	34.8/9.2	4.2/1.1	26	84

and finally cooled down to the reaction temperature in  $N_2$  before the reaction measurement. The concentration of Cl was below the detection limit of the ICP-AES and XPS measurements.

## 2.2. Catalyst characterization

The surface area and the pore diameter of the mesoporous support material and of the different catalysts were determined by  $N_2$  sorption measurements (Autosorb MP1, Quantachrome). The resulting surface areas were calculated using the Brunauer–Emmett–Teller (BET) relation in the  $p/p_0$  range of 0.05–0.30. The pore size distribution was evaluated from the desorption branch of the isotherms, using the procedure developed by Barrett, Joyner and Halenda (BJH) [32]. XRD measurements were performed on a PANalytical MPD PRO instrument, using  $Cu-K_{\alpha}$  radiation ( $\lambda = 0.154$  nm) to evaluate the titania structure and the titania particle sizes. The size and particle distribution of the Au nanoparticles were derived from TEM images obtained in a Philips CM 20 instrument (200 kV). Typically, several hundred Au nanoparticles ( $>400$ ) were evaluated per sample for determining the size distribution of the Au nanoparticles. The relative surface concentrations and the oxidation states of Au, Ti, and O were determined by X-ray photoelectron spectroscopy, using monochromatized  $Al-K_{\alpha}$  radiation for excitation (PHI 5800 ESCA system, Physical Electronic). The binding energies (BEs) were calibrated with respect to the bulk  $Ti(2p_{3/2})$  signal at 459.2 eV for  $Ti^{4+}$  [33]. Subtraction of a Shirley background and peak fitting were performed using a public domain XPS peak fit program (XPSPEAK4.1 by R. Kwok). Thermogravimetry (TGA) measurements were performed on a STA 449C Jupiter instrument (Netsch Gerätebau GmbH). Finally, temperature programmed desorption measurements were performed in a quartz tube micro reactor, which was connected to a mass spectrometer (Atomica IMR-MS 1500). TPD spectra were recorded in a  $N_2$  stream with a temperature ramp of  $5^\circ C\ min^{-1}$ , starting at  $30^\circ C$ .

## 2.3. Activity measurements

The catalytic activity of the catalysts was determined in reaction measurements performed at atmospheric pressure in a quartz tube micro-reactor under differential reaction conditions, using typically 65–70 mg diluted catalyst powder. In order to limit the conversion to values between 5 and 20%, the catalyst was diluted with  $\alpha-Al_2O_3$ , which is not active for CO oxidation under present reaction conditions. The measurements were carried out with a gas flow of 60 N ml  $min^{-1}$  in 1 kPa CO, 1 kPa  $O_2$  and balance  $N_2$  at  $80^\circ C$ . Incoming and effluent gases were analyzed by on-line gas chromatography (Dani GC 86.10HT), using  $H_2$  as carrier gas. High-purity reaction gases (CO: 4.7,  $O_2$ : 5.0 and  $N_2$ : 6.0; Westphalen) were passed through a moisture filter (Varian GC-MS filter CP 17973) to ensure water concentrations of below 0.1 ppm. The reaction rates were determined from the  $CO_2$  partial pressure; for further information on experimental details see ref. [34]. With rates below  $10^{-5}$  mol  $s^{-1}\ cm^{-3}$ , mass and heat transport problems were negligible [35].

## 2.4. Infrared measurements

*In situ* IR measurements were performed by diffuse reflectance infrared fourier transform spectroscopy using a commercial *in situ* reaction cell (Harricks, HV-DR2). The spectra were recorded in a Magna 560 spectrometer (Nicolet) equipped with a MCT narrow band detector. About 20 mg of  $\alpha-Al_2O_3$  diluted catalyst (dilution 1:2) were used as catalyst bed. Typically, 400 scans (acquisition time 3 min) were co-added per spectrum. The intensities were evaluated in Kubelka-Munk units, which are linearly related to the

adsorbate concentration [36]. For possible deviations from this linear behavior see [37]. Background subtraction and normalization of the spectra was performed by subtracting spectra recorded in a flow of  $N_2$  at the reaction temperature directly before starting CO oxidation. To remove changes in the reflectivity of the respective catalysts, the spectra were scaled to similar background intensity at  $2430\ cm^{-1}$ , which did not interfere with any other signals and where the shape of the raw spectrum changed little during the measurements. The gas phase CO signal was removed by subtracting the spectral region of gas phase CO ( $2040$ – $2240\ cm^{-1}$ ) from a spectrum recorded on pure  $\alpha-Al_2O_3$  in CO containing atmosphere, which was verified in test experiments to not adsorb CO under present reaction conditions.

## 3. Results and discussion

### 3.1. Catalyst surface properties

In the following, we present and discuss results on the structure and surface composition of the different Au/TiO<sub>2</sub> catalysts, which were obtained by different techniques including X-ray diffraction,  $N_2$  sorption, thermogravimetric analysis, infrared spectroscopy, transmission electron microscopy as well as X-ray photoelectron spectroscopy.

Based on the characteristic reflections in the diffractograms (a) and (b) of the as-synthesized catalysts in Fig. 1, the synthesis of mesoporous TiO<sub>2</sub> with EGMT and Brij56 or SDS at pH 2 results in anatase. In contrast, for TiO<sub>2</sub> synthesized at pH < 0, only the characteristic rutile reflections are observed (Fig. 1, diffractogram (d)), while for synthesis at pH  $\sim 1.2$  reflections of anatase and rutile coexist (Fig. 1, diffractogram (c)). Obviously, the resulting crystalline phase of TiO<sub>2</sub> depends sensitively on the pH during the synthesis (see also Table 1) [28], in addition to the choice of the titania precursor and the temperature [38]. Additionally, a catalyst supported on commercial, non-porous TiO<sub>2</sub> (P25, Degussa) was characterized (Fig. 1e), which shows reflections of anatase and rutile [26]. Based on the width of the reflections, the crystallite sizes of the mesoporous supports are rather small, about 10 nm for the TiO<sub>2</sub> obtained when using Brij56 as surfactant and about 6–7 nm when using SDS, independent of the crystalline phase of TiO<sub>2</sub>. Since no Au reflections were observed in the raw catalysts by XRD, the Au particles are too small for detection by XRD. For the Au/TiO<sub>2</sub>(1) and Au/TiO<sub>2</sub>(2) catalysts, which are based on the same support material, we obtained BET surface areas of  $106\ m^2\ g^{-1}$  and

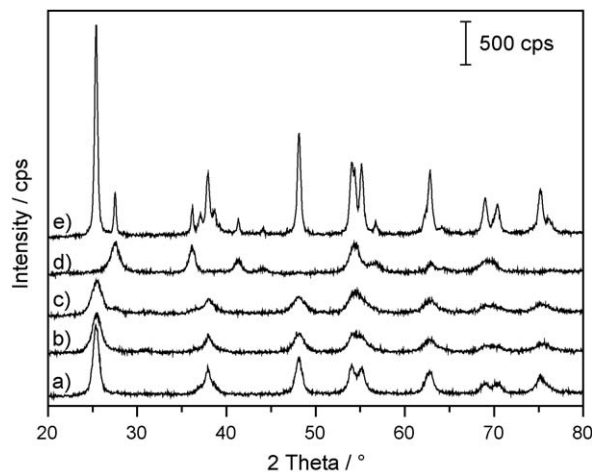


**Fig. 1.** XRD pattern of the different as-synthesized Au/TiO<sub>2</sub> catalysts: (a) Au/TiO<sub>2</sub>(2), which is supported on the same material as catalyst (1), (b) Au/TiO<sub>2</sub>(3), (c) Au/TiO<sub>2</sub>(4), (d) Au/TiO<sub>2</sub>(5), (e) Au/TiO<sub>2</sub>(P25).

pore diameters of 8 nm. The interaction of SDS as the structure-directing agent in the synthesis protocol with the growing titania species is due to its ionic character completely different from that of the previously applied Brij56 as a non-ionic surfactant (samples (1) and (2)). In our case, this interaction results in larger specific surface areas of 175, 240 and 160 m<sup>2</sup> g<sup>-1</sup> for samples (3)–(5), respectively.

The thermal stability of the different unconditioned catalysts was characterized by TGA. With increasing BET surface area, the weight loss of the mesoporous catalysts increased (see Table 1). This weight loss is mainly attributed to the desorption of molecularly adsorbed water and recombination of OH groups [39], whose amount increases with increasing BET surface area. At higher temperatures (>500 °C), the catalyst weight loss (0.7–2.6%, see Table 1) is caused by reactive desorption of carbon containing species, which are residuals from the TiO<sub>2</sub> synthesis (see also Section 3.2). These species are also visible in IR spectra recorded on the different catalysts (Fig. 2). Prior to the IR measurements, the catalysts were dried at 100 °C for 15 h and calcined at 400 °C. Signals at 2352 and 1358 cm<sup>-1</sup> belong to the carbon containing species, which are not observed on the P25 based catalyst (Fig. 2, spectrum (e)). The first signal is usually related to gas phase CO<sub>2</sub> resulting from CO oxidation (CO<sub>2</sub> was not present in the gas-mixture). In all cases, except the rutile catalyst (5), vibrations at ~1617 and 2600–3500 cm<sup>-1</sup> as well as at 3724 and 3672 cm<sup>-1</sup> belong to adsorbed water and individual OH groups, respectively. For the catalyst (5), isolated OH groups are observed at 3737 and 3672 cm<sup>-1</sup>. (Note that the signals in the C–H region at 2700–3000 cm<sup>-1</sup>, which are normally indicative of adsorbed formates, were caused by contaminants on the IR mirrors.)

After calcination at 400 °C for 30 min, the catalysts were characterized by XPS and TEM. For all catalysts, Au is mainly present as metallic Au<sup>0</sup> species [22,40]. Similar results were also obtained for an XPS measurement on the dried-plus-calcined Au/

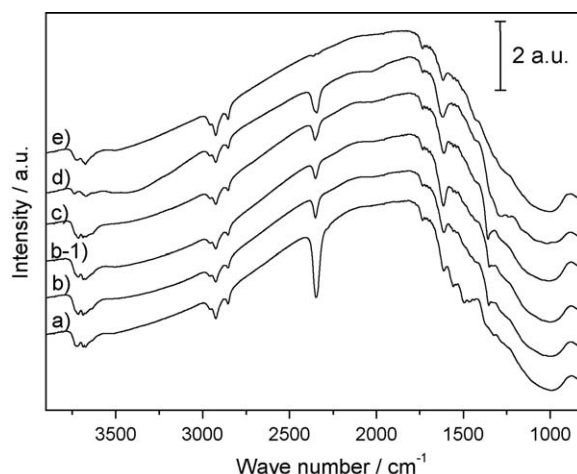


**Fig. 2.** DRIFTS spectra (raw data) of the different Au/TiO<sub>2</sub> catalysts recorded after 15 h drying in N<sub>2</sub> at 100 °C followed by calcination at 400 °C (30 min, 10% O<sub>2</sub>/N<sub>2</sub>): (a) Au/TiO<sub>2</sub>(2), which is supported on the same material as catalyst (1), (b) Au/TiO<sub>2</sub>(3), (b-1) Au/TiO<sub>2</sub>(3) after calcination without drying, (c) Au/TiO<sub>2</sub>(4), (d) Au/TiO<sub>2</sub>(5), (e) Au/TiO<sub>2</sub>(P25).

TiO<sub>2</sub>(3) catalyst, indicating that the drying procedure has no effect on the surface composition of the Au nanoparticles. A similar behavior is also assumed for the other dried-plus-calcined catalysts. Furthermore, the  $I_{\text{Au}(4f)}/I_{\text{Ti}(2p)}$  intensity ratio decreases with increasing BET surface area (see Table 2). The TEM images of the samples revealed small TiO<sub>2</sub> crystallites whose size varied between 5 and typically 15 or 30 nm for the Brij56 based catalysts (1) and (2), respectively, while the crystallites are smaller for the SDS based catalysts (3)–(5), comparable to the XRD results. The TiO<sub>2</sub> crystallites are connected via grain boundaries, forming an open framework with pores between the crystallites. Thorough

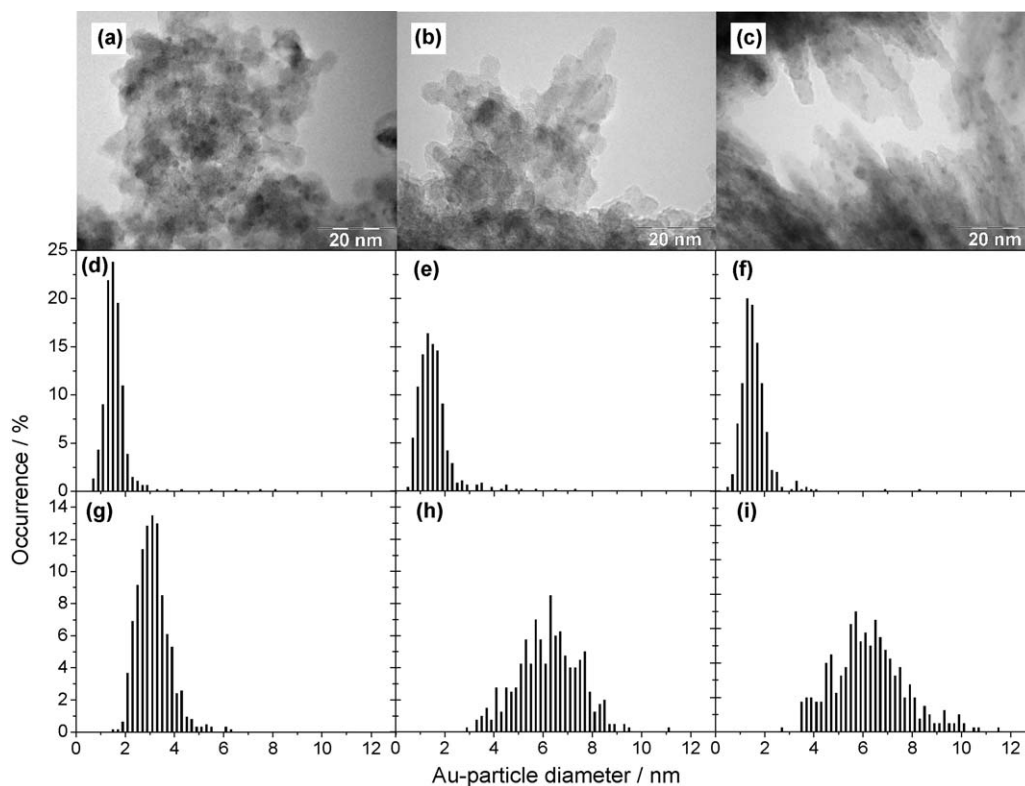


**Fig. 3.** TEM images (a)–(c) and Au particle size distributions (d)–(i) of the different Au/TiO<sub>2</sub> catalysts (3)–(5) after synthesis (a)–(f) and after calcination at 400 °C (30 min, 10% O<sub>2</sub>/N<sub>2</sub>) (g)–(i). From left to right panel: Au/TiO<sub>2</sub>(3), Au/TiO<sub>2</sub>(4), Au/TiO<sub>2</sub>(5).



TEM investigations have shown that in the Au/TiO<sub>2</sub>(1)–(5) catalysts rutile and anatase can be distinguished morphologically; anatase crystallizes in nanoparticles and rutile in nanowhiskers (see also ref. [41]). Examples of these samples are shown in the TEM images in Fig. 3a–c. Both morphologies are present on the catalyst (4), which is a mixture between anatase and rutile (see Fig. 3b), comparable results were reported by Wang et al. [14]. In contrast to the mesoporous samples, the rutile phase of P25 does not crystallize in nanowhiskers. In addition to the morphology of the TiO<sub>2</sub> support, the TEM images revealed a homogeneous distribution of the Au nanoparticles (Fig. 3). The as synthesized Au catalysts (3)–(5) show the same Au particle size distribution of 1.6 nm (Fig. 3d–f), independent of the crystalline phase of the support. Calcination of the samples at 400 °C leads to Au nanoparticle growth. The resulting Au nanoparticle size distributions yield mean particle sizes between  $3.0 \pm 0.7$  and  $4.1 \pm 0.8$  nm for the different mesoporous anatase supported catalysts (1)–(3) (Fig. 3g, Table 2), which is comparable to our previously reported results [12]. A comparable Au particle size of  $2.9 \pm 0.7$  nm was found for the P25 based Au/TiO<sub>2</sub> catalyst. In contrast, the mesoporous catalysts supported on rutile or rutile/anatase reveal a larger Au particle size of  $6.1 \pm 1.5$  nm (Fig. 3d and f). Here the Au particle sizes are comparable to the TiO<sub>2</sub> crystallite and pore sizes. This match between Au particle size and TiO<sub>2</sub> pore size is compatible with the proposal of an extended Au–TiO<sub>2</sub> interface with multiple contacts by Pietron et al. [8]. Finally, comparative TEM measurements on the dried plus calcined Au/TiO<sub>2</sub>(3) showed no significant deviation in the Au nanoparticle size compared to the purely calcined catalyst, indicating that also the resulting Au particle size is not affected by the drying procedure.

Apparently, the same Au loading and calcination procedures lead to larger Au nanoparticles on the mixed or on the rutile support than on the anatase support. Since before calcination the Au particle sizes were comparable for all catalysts (1.6 nm diameter, see above), this must be related to a better stabilization of the Au nanoparticles on the anatase support during calcination. Our data for anatase and P25 supported catalysts disagree with the findings by Schwartz et al., who reported a more pronounced Au particle growth upon calcination of mesoporous Au/TiO<sub>2</sub> than on non-porous supports, with a mean particle size of  $\sim 10$  nm for the mesoporous catalysts upon calcination at 300 °C compared to 1–3 nm on the non-porous supports [25]. Comparing mesoporous rutile and anatase supported Au/TiO<sub>2</sub> catalysts, Yan et al. found that calcination of these Au/TiO<sub>2</sub> catalysts at 300 °C leads to comparable Au particle sizes of  $>5$  nm [26]. The surface areas of the oxides, however, differed considerably (rutile  $77 \text{ m}^2 \text{ g}^{-1}$ , anatase  $225 \text{ m}^2 \text{ g}^{-1}$ ). On the other hand, Comotti et al. reported a lower Au particle size of  $\sim 3$  nm for mesoporous rutile and anatase supported catalysts (rutile  $108 \text{ m}^2 \text{ g}^{-1}$ , anatase  $327 \text{ m}^2 \text{ g}^{-1}$ ) after similar calcination treatment [27], which comes close to the values we obtained for the anatase supported catalysts, while for the rutile supported catalyst we obtain Au particle sizes more comparable to those of Yan et al. [26].

In total, the above measurements lead to the following results and conclusions:

- (i) Using EGMT and Brij56 or SDS as surfactants, the synthesis of mesoporous TiO<sub>2</sub> at pH-values of 0 and 2 results in the formation of rutile and anatase, respectively, while at intermediate pH values a mixture of rutile and anatase is obtained.
- (ii) The mesoporous TiO<sub>2</sub> crystallizes in anatase nanoparticles and rutile nanowhiskers, respectively. These contain carbon impurities from the TiO<sub>2</sub> synthesis.
- (iii) The amount of water on the as-synthesized samples increases with increasing surface area.

- (iv) The Au nanoparticles are homogeneously distributed on the mesoporous TiO<sub>2</sub> support as well as on P25, both within the pores and on the outer surface of the TiO<sub>2</sub> framework.
- (v) After calcination at 400 °C, Au is mainly present as metallic species, and 3 nm Au nanoparticles are observed on Au/anatase and Au/P25. On the mesoporous Au catalysts supported on rutile or rutile–anatase mixtures, the Au particles are about 6 nm in diameter.

### 3.2. Influence of a catalyst drying step on the CO oxidation behavior

In recent experiments we had shown that the activity and deactivation behavior of P25 based Au/TiO<sub>2</sub> catalysts can be sensitively influenced by the content of adsorbed H<sub>2</sub>O and hydroxyl groups and by trace impurities of H<sub>2</sub>O in the gas mixture [29]. In the absence of water in the gas feed and after extensive drying prior to calcination, the initial activity was found to increase substantially. On the other hand, also the deactivation increased to about 70% during reaction at 80 °C over 1000 min, compared to 25% without drying. In order to test for similar effects on the mesoporous catalysts, the CO oxidation activity was measured after different pre-treatment procedures, including (i) calcination at 400 °C (N0–O400), (ii) drying in N<sub>2</sub> at 100 °C for 1.5 h followed by calcination at 400 °C (N1.5–O400), and (iii) drying in N<sub>2</sub> at 100 °C for 15 h followed by calcination at 400 °C (N15–O400) (see Fig. 4). The top panel depicts the evolution of the activity of the Au/TiO<sub>2</sub>(3) catalyst under these reaction conditions, described by turn-over frequencies under differential reaction conditions (Fig. 4a). The bottom panel shows the deactivation on a relative scale, normalized to an initial activity of 100% (Fig. 4b). Similar to our previous observations on P25–TiO<sub>2</sub> supported Au/TiO<sub>2</sub> catalysts [29], the drying procedure has a pronounced effect on the activity and the deactivation behavior. The initial activity increases with increasing

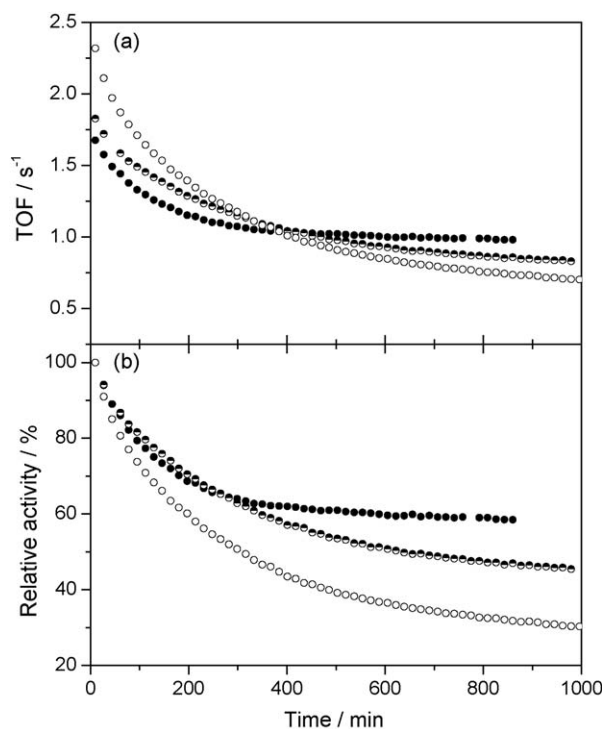


**Fig. 4.** Evolution of turn-over frequencies (TOF) for CO oxidation (a) and the relative conversion (b) during reaction in 1 kPa CO, 1 kPa O<sub>2</sub>, balance N<sub>2</sub> at 80 °C on Au/TiO<sub>2</sub>(3) after: (●) calcination at 400 °C, (◐) 1.5 h drying in N<sub>2</sub> at 100 °C followed by calcination at 400 °C and (○) 15 h drying in N<sub>2</sub> at 100 °C followed by calcination at 400 °C.

drying time in the following order: N0-O400 < N1.5-O400 < N15-O400, while this order is reversed when comparing the activities after 600 min reaction and later. Hence, similar to the P25-based Au/TiO<sub>2</sub> catalyst [29], drying results in a higher initial activity of the catalyst, but also in a higher deactivation during CO oxidation. The different behavior of the various catalysts can result from various effects, including differences in the amount/nature of the surface species initially adsorbed on the catalysts or differences in the Au particle size caused by the pre-treatment procedures. The latter effect, drying induced Au particle sintering, can be excluded, since TEM measurements after N0-O400 and N15-O400 revealed comparable Au particle sizes of  $3.0 \pm 0.7$  nm and  $3.1 \pm 1.0$  nm, respectively. Also Au particle sintering during reaction was found to be absent in previous studies on P25-TiO<sub>2</sub> based Au/TiO<sub>2</sub> catalysts [29], and TEM measurements on a mesoporous Au/TiO<sub>2</sub> catalyst (Au/TiO<sub>2</sub>(3)) after 1000 min reaction, which yielded a Au particle size of  $3.0 \pm 0.8$  nm, led to similar conclusions.

In previous studies on non-porous and mesoporous TiO<sub>2</sub> supported Au/TiO<sub>2</sub> catalysts, the formation of surface carbonates and related species was identified as the main source of their deactivation during CO oxidation [12,40,42–44]. Therefore, the effect of catalyst drying on the nature and amount of adsorbed surface species on the Au/TiO<sub>2</sub>(3) catalysts was investigated, employing temperature programmed desorption and IR measurements. In the latter measurements, we followed the temporal evolution of the intensities of different peaks related to adsorbed species during the CO oxidation reaction on the Au/TiO<sub>2</sub>(3) catalyst after different pre-treatments. TPD spectra recorded on the TiO<sub>2</sub>(3) support and on differently pre-treated Au/TiO<sub>2</sub>(3) catalysts are presented in Fig. 5, following the O<sub>2</sub> (Fig. 5a), CO<sub>2</sub> (Fig. 5b) and H<sub>2</sub>O (Fig. 5c) partial pressures (curve (1): TiO<sub>2</sub>(3) unconditioned support, curve (2): unconditioned Au/TiO<sub>2</sub>(3) catalyst, curve (3): Au/TiO<sub>2</sub>(3) catalyst after drying in N<sub>2</sub> at 100 °C for 15 h, curve (4): Au/TiO<sub>2</sub>(3) catalyst after calcination at 400 °C for 30 min, and curve (5): Au/TiO<sub>2</sub>(3) catalyst after drying in N<sub>2</sub> at 100 °C for 15 h followed by calcination at 400 °C for 30 min). Note that in all cases the mesoporous TiO<sub>2</sub> was calcined at 400 °C for 4 h, prior to the TPD measurement and prior to Au loading, and subsequently stored in air at room temperature. Therefore subsequent calcination of the Au loaded catalyst did not change the support material any more. H<sub>2</sub>O desorption from pure TiO<sub>2</sub> shows a pronounced desorption peak at about 140 °C (Fig. 5c, curve (1)), which can result either from desorption of molecularly adsorbed water or from recombination of adsorbed or bulk OH groups [39]. CO<sub>2</sub> and O<sub>2</sub> desorption occurs at about 615 °C (CO<sub>2</sub>, 33  $\mu\text{mol g}_{\text{cat}}^{-1}$ ) or in an increasing desorption signal at temperatures close to the maximum temperature in the scan of 700 °C (O<sub>2</sub>, 65  $\mu\text{mol g}_{\text{cat}}^{-1}$ ), respectively. These latter desorption peaks are attributed to the decomposition of carbon containing species. Considering that on P25 such peaks are not observed, these must be residuals from the TiO<sub>2</sub> synthesis. The formation of high temperature desorption peaks is in good agreement with the TGA results described in Section 3.1 (see also Table 1), where an additional weight loss between 500 and 900 °C was observed. Going to the Au/TiO<sub>2</sub>(3) catalysts, the amount of these species remains similar, independent of the pre-treatment (see curves (2)–(5)). Water represents the dominant desorption product on the unconditioned catalyst, accompanied by additional O<sub>2</sub> and CO<sub>2</sub> desorption. These findings are in good agreement with the results of Yan et al., who observed comparable desorption traces on an unconditioned, mesoporous 13 wt.% Au/anatase catalyst [26]. In addition to the high temperature peak (see above), CO<sub>2</sub> desorbs in a broad peak with maxima at about 105 °C (shoulder), 195 °C, 350 °C and 430 °C (31  $\mu\text{mol g}_{\text{cat}}^{-1}$  of CO<sub>2</sub>), O<sub>2</sub> desorbs in a peak centered at about 365 °C (57  $\mu\text{mol g}_{\text{cat}}^{-1}$  of O<sub>2</sub>), in addition to the O<sub>2</sub> partial pressure increase at high temperatures close to 700 °C described above.

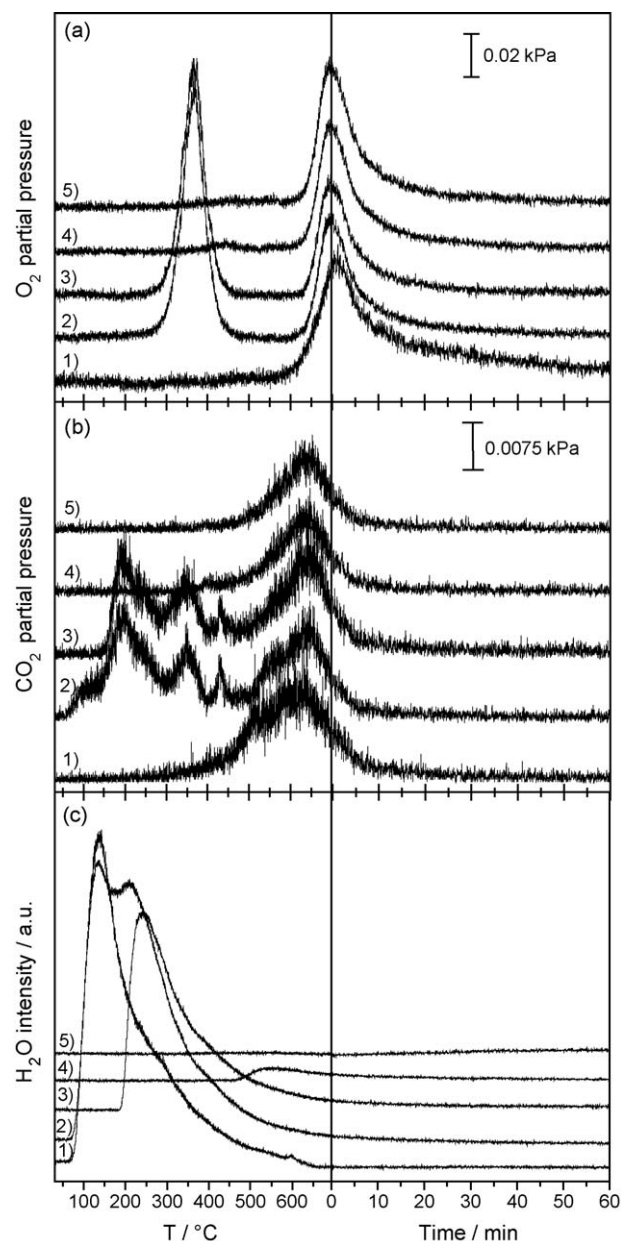


**Fig. 5.** TPD measurements on pure TiO<sub>2</sub> used for catalyst (3) curve (1) and on Au/TiO<sub>2</sub>(3) catalysts (curves (2)–(5)) after different treatments: (2) unconditioned, (3) after 15 h drying in N<sub>2</sub> at 100 °C, (4) after 30 min calcination at 400 °C, and (5) after 15 h drying in N<sub>2</sub> at 100 °C followed by 30 min calcination at 400 °C. From top to bottom: (a) O<sub>2</sub> desorption, (b) CO<sub>2</sub> desorption and (c) H<sub>2</sub>O desorption.

These additional desorption features must be related to changes in the TiO<sub>2</sub> surface introduced by the Au deposition process or to processes activated by the presence of Au. The desorbing oxygen can result from the reduction of oxidic Au<sup>n+</sup> species to metallic gold and/or from the reduction of titanium oxides, while the desorbed CO<sub>2</sub> is again attributed to the decomposition of surface carboxylate/carbonate species on the titania support, which were formed upon interaction of the catalyst with air during catalyst transport. Comparison with oxygen desorption from the pure TiO<sub>2</sub> support indicates that if oxygen formation in the low temperature peak results from titania, the formation of oxygen vacancies must occur in the vicinity of Au nanoparticles (Au assisted O vacancy formation). The desorption of H<sub>2</sub>O is more pronounced compared to the pure TiO<sub>2</sub>, with an additional desorption peak at 210 °C. Obviously, the new peak at 210 °C is also related to the presence of

the Au nanoparticles, and tentatively attributed to the recombination of OH groups on adsorption sites adjacent to the Au nanoparticles.

After drying the catalyst at 100 °C for 15 h in N<sub>2</sub>, the amount of adsorbed water/hydroxyl species is reduced (Fig. 5c, curve 3), and only a single peak at about 240 °C is observed. The shift to higher temperature compared to the non-treated Au/TiO<sub>2</sub>(3) catalyst (H<sub>2</sub>O desorption maximum at 210 °C) is most likely due to (reactive) desorption of the lower temperature species during the preceding drying step at 100 °C. The desorption characteristics and the amount of desorbed O<sub>2</sub> and CO<sub>2</sub> are not affected by the drying procedure.

*In situ* calcination of the catalyst (30 min, 400 °C) with and without preceding drying leads to the complete removal of the additional O<sub>2</sub> and CO<sub>2</sub> containing species formed on the surface upon Au deposition, as evidenced by the absence of O<sub>2</sub> and CO<sub>2</sub> desorption peaks below 600 and 400 °C, respectively. The O<sub>2</sub> and CO<sub>2</sub> desorption peaks appearing at higher temperatures, which were observed also during desorption from the pure (calcined) TiO<sub>2</sub> support, appear again and are explained accordingly (decomposition of carbon containing species formed during the TiO<sub>2</sub> synthesis). Also H<sub>2</sub>O desorption is strongly reduced. A low desorption signal appears at temperatures above 450 °C on the calcined sample, while on the dried-plus-calcined catalyst water desorption cannot be observed any more. Hence, the extensive drying procedure prior to calcination reduces the amount of OH species on the catalyst surface significantly. This is also consistent with the results of the DRIFTS measurements discussed in the preceding Section 3.1, which showed that even after (*in situ*) N15-O400 pre-treatment OH groups and water are present on the catalyst surface [39]. A higher water signal is also observed in DRIFT spectra of the N0-O400 catalyst compared to the dried-plus-calcined (N15-O400) catalyst (Fig. 2).

The accumulation of adsorbed surface species during the reaction and the influence of the catalyst pre-treatment thereon were characterized by *in situ* DRIFTS measurements performed during reaction on a calcined (N0-O400) Au/TiO<sub>2</sub>(3) catalyst (Fig. 6a–c) and on a dried plus calcined (N15-O400) Au/TiO<sub>2</sub>(3) catalyst (Fig. 6d–f). The sequences of DRIFT spectra indicate that the additional drying procedure does not affect the nature of the

surface species formed during reaction at 80 °C. The characteristic peaks at 3724 and 3675 cm<sup>-1</sup> are attributed to isolated OH groups [45–47]), the broad band at 3500–2600 cm<sup>-1</sup>, peaks at 2344 and 2356 cm<sup>-1</sup>, and a peak at 2123–2133 cm<sup>-1</sup> are associated with adsorbed water, gaseous CO<sub>2</sub> and CO adsorbed on metallic Au, respectively [48–50]. The band for CO<sub>ad</sub> appears at slightly higher wave number compared to that on P25 based Au/TiO<sub>2</sub> catalysts (2118 cm<sup>-1</sup> [12]), which agrees with our previous results on mesoporous Au/TiO<sub>2</sub> catalysts [12] and points to subtle differences in the interaction between Au and the two different TiO<sub>2</sub> substrates. Peaks in the range 2154–2116 cm<sup>-1</sup> have previously been assigned to CO adsorbed on partly positively charged Au<sup>δ+</sup> species [48,51]. Considering the pre-treatment conditions of the catalysts in the present study (calcination at 400 °C) and the Au particle size of around 3 nm and more in diameter, we find the formation of positively charged Au<sup>δ+</sup> species rather unlikely under present reaction conditions (see also previous *in situ* X-ray absorption studies [52], for the importance of pre-treatment conditions see also [51]). Therefore we prefer to assign the band at 2123–2133 cm<sup>-1</sup> to CO adsorption on possibly modified, but still metallic Au sites. A set of vibrational features in the range between 1200 and 1700 cm<sup>-1</sup> is assigned to adsorbed water (~1617 cm<sup>-1</sup>) and to C=O and OCO vibrations of carbonates and carboxylates [49,50,53]. The C=O stretch vibration at ~1564 cm<sup>-1</sup> is attributed to bidentate carbonates, while the peak at ~1432 cm<sup>-1</sup> is related to the asymmetric stretch vibration  $\nu_{as}(\text{COO})$  of monodentate carbonates [50,53]. The symmetric stretch vibration  $\nu_s(\text{COO})$  of monodentate carbonates (1359 cm<sup>-1</sup>) is hidden under the vibration features of carbon containing species resulting from the TiO<sub>2</sub> synthesis (see above). The same holds true for the asymmetric stretch vibration of carboxylates, which should give rise to a peak in the range 1560–1620 cm<sup>-1</sup> [53]. The symmetric stretch vibration of the adsorbed carboxylates, which should appear at ~1406 cm<sup>-1</sup>, is covered by a peak related to monodentate carbonates [40].

The temporal evolution of the peak intensities related to the different CO<sub>ad</sub>, CO<sub>2</sub> and carbonate species is qualitatively comparable for both treatments, with only slight differences in the quantitative intensity variations (Fig. 6). During the reaction, the CO<sub>ad</sub> and CO<sub>2</sub> intensities decrease and that of the carbonate

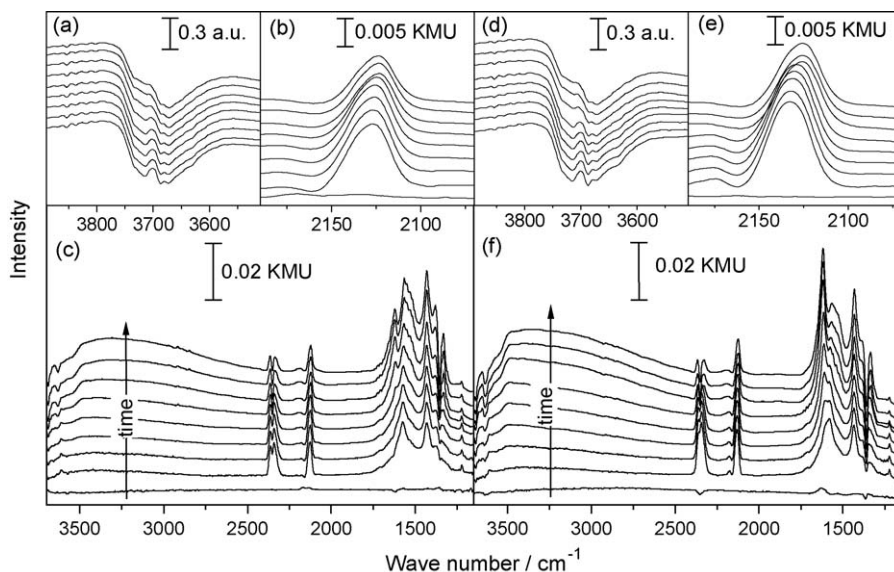


**Fig. 6.** Selected spectra from a series of DRIFT spectra recorded during CO oxidation (1 kPa CO, 1 kPa O<sub>2</sub>, balance N<sub>2</sub>, 80 °C) on a Au/TiO<sub>2</sub>(3) catalyst after calcination at 400 °C (left panel (a)–(c)) and after 15 h drying in N<sub>2</sub> at 100 °C followed by calcination at 400 °C (right panel (d)–(f)) (reaction times: 0, 5, 10, 15, 30, 60, 240, 600 and 1000 min). Each panel shows the complete spectrum (c), (f) as well as details of the O–H (a), (d) and C–O (b), (e) spectral regions. Note that in (a) and (d) raw data are shown, while the full spectra are background subtracted.



species increases. These trends are consistent with previously reported results [40]. Hence, also for the mesoporous Au/TiO<sub>2</sub> catalyst, the deactivation is correlated with the build-up of carbonates, similar to earlier proposals for the deactivation process of P25-based Au/TiO<sub>2</sub> catalysts [22,40,42].

In addition to these trends, the intensity of the water signal at  $\sim 1617\text{ cm}^{-1}$  increases with ongoing reaction, while that of the OH signal at  $3725\text{ cm}^{-1}$  decreases. This points to OH consumption and H<sub>2</sub>O formation during the reaction, and is again comparable to previous observations on P25-TiO<sub>2</sub> based catalysts [22,54]. The consumption of OH groups is even stronger on the dried plus calcined N15-O400 catalyst (Fig. 6d–f) than on the calcined N0-O400 catalyst (Fig. 6a–c). We explain this difference by the larger amount of adsorbed H<sub>2</sub>O on the N0-O400 catalyst. Therefore, on the calcined N0-O400 sample less H<sub>2</sub>O formation is required for reaching the steady-state concentration of adsorbed water than on the dried plus calcined N15-O400 catalyst. The shift from adsorbed hydroxyls to adsorbed water during the CO oxidation reaction was explained earlier by (oxidative) displacement of surface hydroxyl groups in the reaction mixture [55], or an equilibrium between hydroxyl groups and water [46,56].

Our IR, TPD and activity measurements clearly indicate that the drying procedure affects the CO oxidation activity and deactivation behavior via the different amounts of pre-adsorbed water on the catalysts before CO oxidation. The influence of H<sub>2</sub>O trace impurities or controlled amounts of H<sub>2</sub>O in the reaction gas was already investigated in numerous studies [49,50,54,57,58]. Daté and Haruta found that the steady-state CO activity increases with small amounts of H<sub>2</sub>O in the gas-mixture (up to 200 ppm), while higher water concentrations have a negative influence [54]. The increase with activity for small amounts of H<sub>2</sub>O in the reaction gas mixture is consistent with our results, where the highest steady-state activity was observed on the non-dried catalyst, which has the highest coverage of adsorbed water on the catalyst (see TPD,

DRIFTS measurements). In an experiment more comparable to our measurements, Debeila et al. followed the CO oxidation activity upon injection of water to a dry gas-mixture, after 25 min reaction time [59]. They observed an initial decrease in activity, followed by a slow increase until finally a higher activity compared to the initial one was reached. The initial decrease in activity reflects the lower activity reported by Daté and Haruta for higher water contents [54], the subsequent increase to an even higher activity than the original one agrees with our observation of a higher steady-state activity on the non-dried catalyst.

### 3.3. Influence of different supports on the CO oxidation activity

The activity and deactivation of the different Au/TiO<sub>2</sub> catalysts with time during 1000 min CO oxidation in a standard reaction mixture (1 kPa CO, 1 kPa O<sub>2</sub>, rest N<sub>2</sub>) at 80 °C are illustrated in Fig. 7a–d. All catalysts were dried and calcined (N15-O400 pre-treatment) before reaction. The left panels (Fig. 7a and c) depict the evolution of the activity, as described by the Au mass specific rate under differential reaction conditions. The right panels (Fig. 7b and d) show the deactivation on a relative scale, normalized to an initial activity of 100%. In all cases, the activity decreases exponentially to a near steady-state value. In the upper panels (Fig. 7a and b), we compare the activity of the anatase supported catalysts Au/TiO<sub>2</sub>(1)–(3) with the standard P25 supported catalyst. The highest activities were observed for the mesoporous Au/TiO<sub>2</sub>(1) and Au/TiO<sub>2</sub>(2) catalysts with the lower BET surface area (see Tables 1 and 2). The activity of the mesoporous Au/TiO<sub>2</sub>(3) catalysts with the higher BET surface area is lower, but still slightly higher than that of the P25-TiO<sub>2</sub> based catalyst. The steady-state activities of the latter catalysts amount to about 30% of that of the lower surface area catalysts (1) and (2). Because of the rather similar Au particle sizes, the trends are maintained if we compare the inherent, TOF based activities of the different catalysts, which

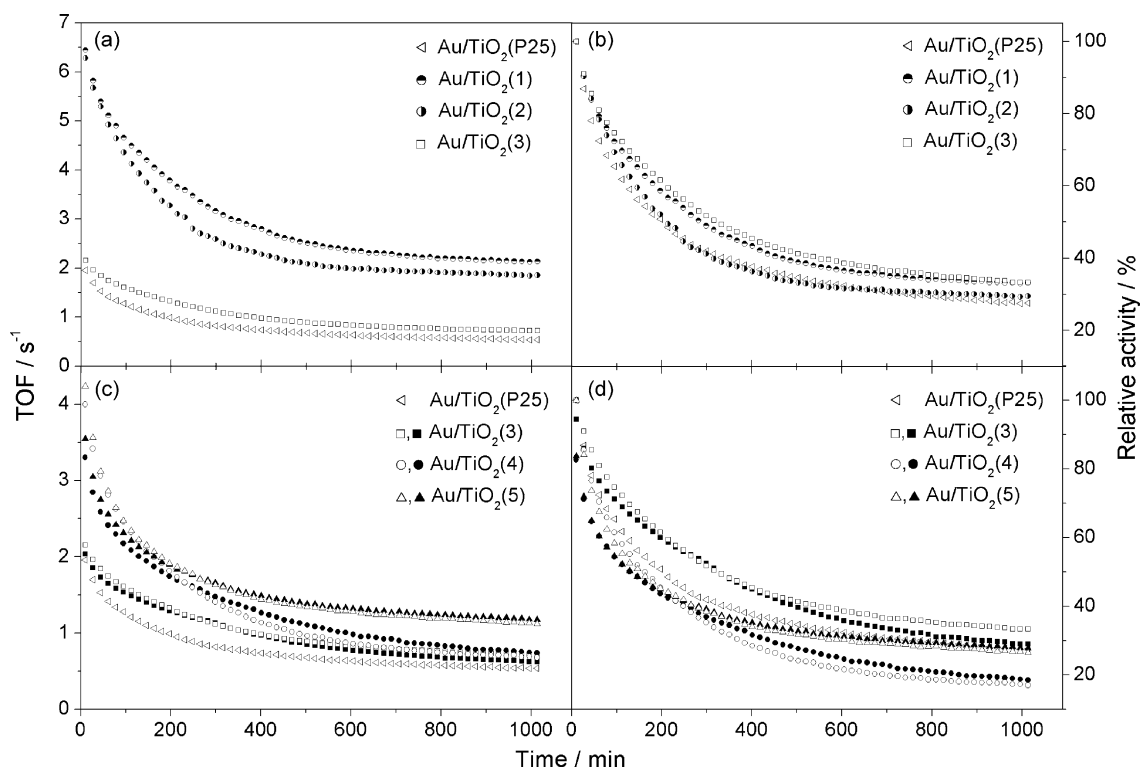


**Fig. 7.** Evolution of (a), (c) turn-over frequencies (TOF) for CO oxidation and of (b), (d) the relative activity during 1000 min CO oxidation (1 kPa CO, 1 kPa O<sub>2</sub>, balance N<sub>2</sub>, 80 °C) on various Au/TiO<sub>2</sub> catalysts: (◁) Au/TiO<sub>2</sub>(P25), (●) Au/TiO<sub>2</sub>(1), (○) Au/TiO<sub>2</sub>(2), (◻) Au/TiO<sub>2</sub>(3), (◊) Au/TiO<sub>2</sub>(4), and (▲) Au/TiO<sub>2</sub>(5). Filled symbols: CO oxidation on Au/TiO<sub>2</sub>(3)–(5) after reaction and subsequent re-calcination.



are around  $2 \text{ s}^{-1}$  for the low surface area catalysts (1) and (2), and about  $0.6 \text{ s}^{-1}$  for the less active high surface area catalyst (3) and the P25 supported catalyst (steady-state activities, see Table 2).

The reaction characteristics of the rutile supported Au/TiO<sub>2</sub>(5) catalyst and of the mixed anatase and rutile supported catalyst (4) are displayed in the bottom graphs in Fig. 7c and d, again together with the P25-TiO<sub>2</sub> supported standard catalyst for comparison. These measurements show about similar steady-state activities for the catalyst (5) and the P25 supported catalyst, while the activity of the mixed rutile/anatase supported catalyst (4) is significantly lower, being the lowest of all catalysts investigated (steady-state activities, see Table 2). Due to the significantly larger Au nanoparticles of the rutile supported Au/TiO<sub>2</sub>(5) and the mixed rutile/anatase supported Au/TiO<sub>2</sub>(4) catalysts, the TOF based activities, however, are somewhat higher for the latter catalyst, with about  $0.7$  and  $1.1 \text{ s}^{-1}$ , than for the P25-based catalyst ( $0.5 \text{ s}^{-1}$ ) and the high surface area anatase supported catalyst (3) ( $0.7 \text{ s}^{-1}$ ) (steady-state activities, see Table 2). The deactivation of about 70–80% over 1000 min reaction is comparable for all catalysts. Hence, the anatase based catalysts (1) and (2) showed a clearly higher activity than the rutile based catalyst (5), both in Au mass normalized rates and in the TOF number. Comparison of the rutile supported Au/TiO<sub>2</sub>(5) catalyst ( $160 \text{ m}^2 \text{ g}^{-1}$ ) with the slightly higher surface area anatase supported Au/TiO<sub>2</sub>(3) catalyst ( $175 \text{ m}^2 \text{ g}^{-1}$ ), in contrast, shows only small differences in the Au mass normalized rates, and a higher TOF based activity of the rutile supported Au/TiO<sub>2</sub>(5) catalyst.

The higher activity of the catalysts (1) and (2) compared to that of the P25 based catalyst resembles our previous results, where we found higher initial and steady-state activities for mesoporous Au/TiO<sub>2</sub> catalysts prepared using Brij56 and EGMT as surfactants, compared to that of a P25 based catalyst [12]. The deactivation of 67–72% during 1000 min on stream, however, is much more pronounced than that reported in the previous study (deactivation about 12–25%). This difference results, however, from the additional drying procedure (see Fig. 4 and Section 3.2) rather than from inherent differences in the mesoporous catalysts in the two studies, and similar differences were observed also for

standard Au/TiO<sub>2</sub> catalysts supported on P25 [29]. Comparing the mesoporous Au/TiO<sub>2</sub> catalysts with the P25 based Au/TiO<sub>2</sub> catalyst, the deactivation of the mesoporous catalysts was slightly lower, which may be related to the higher surface area, leading to a lower density of the carbonate adlayer [12]. The differences, however, are rather small.

The observation of a higher activity of the mesoporous Au/TiO<sub>2</sub> catalysts resembles earlier findings by Pietron et al., who reported a Au mass normalized activity of the mesoporous Au catalysts comparable to that of the most active Au/TiO<sub>2</sub> catalysts described in the literature [8]. They explained the higher activity of the mesoporous catalysts by the increased contact between the Au nanoparticles (mean diameter 5.5 nm) and the TiO<sub>2</sub> anatase substrate (mean pore size 10–12 nm), with contact at more than one position, which they suggested to lead to shorter diffusion pathways of CO<sub>ad</sub> to the interface region between Au nanoparticles and TiO<sub>2</sub>.

The tendency to a lower activity for anatase supported Au/TiO<sub>2</sub> catalysts with higher surface areas (catalyst Au/TiO<sub>2</sub>(3):  $175 \text{ m}^2 \text{ g}^{-1}$ ), catalysts Au/TiO<sub>2</sub>(1) and (2):  $\sim 100 \text{ m}^2 \text{ g}^{-1}$ ) resembles the observations of Moreau et al. [24]. Investigating the effect of the surface area on anatase supported Au catalysts in temperature screening experiments, they found the highest CO oxidation activity on a Au/TiO<sub>2</sub> catalyst with a rather low BET surface area, and an activity decrease with increasing BET surface area in the order  $37 \text{ m}^2 \text{ g}^{-1} > 45 \text{ m}^2 \text{ g}^{-1} > 90 \text{ m}^2 \text{ g}^{-1} > 240 \text{ m}^2 \text{ g}^{-1} > 305 \text{ m}^2 \text{ g}^{-1}$ . On the other hand, these authors reported a higher activity, by a factor of two, for a Au/rutile catalyst ( $100 \text{ m}^2 \text{ g}^{-1}$ ) compared to a Au/anatase catalyst of similar surface area ( $90 \text{ m}^2 \text{ g}^{-1}$ ). Based on temperature screening measurements on Au/rutile, Au/anatase and Au/P25 catalysts, Comotti et al. concluded that the crystalline phase of TiO<sub>2</sub> has no significant effect on the CO oxidation activity [27]. (It should be noted the surface areas of the different catalysts used in these latter measurements differed widely,  $327 \text{ m}^2 \text{ g}^{-1}$  for the Au/anatase catalyst,  $108 \text{ m}^2 \text{ g}^{-1}$  for the Au/rutile catalyst, and  $47 \text{ m}^2 \text{ g}^{-1}$  for the Au/P25 catalyst). Schwarz et al. [25] and Yan et al. [26] reported a higher activity ( $T_{50}$  value or TOF number, respectively) of anatase supported Au/TiO<sub>2</sub> catalysts compared to rutile based

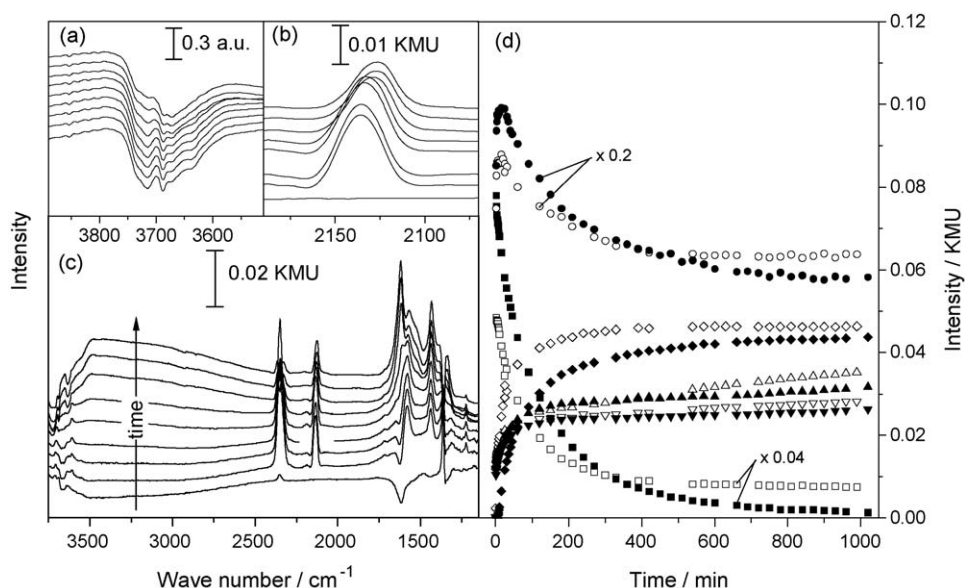


**Fig. 8.** Left panel, (a)–(c): Selected spectra from a series of DRIFT spectra recorded during the CO oxidation (1 kPa CO, 1 kPa O<sub>2</sub>, balance N<sub>2</sub>, 80 °C) on a Au/TiO<sub>2</sub>(3) after re-calcination at 400 °C (reaction times: 0, 5, 10, 15, 30, 60, 240, 600 and 1000 min). Each panel shows the complete spectrum (c) as well as details of the O–H (a) and C–O spectral regions (b). Note that in (a) raw data are shown, while the full spectra are background subtracted. Right panel (d): Temporal evolution of the CO<sub>ad</sub> (○, ●) and CO<sub>2</sub> peak area (□, ■) as well as of the peak intensities at 1617 cm<sup>-1</sup> (water: ▽, ▼), 1564 cm<sup>-1</sup> (bidentate carbonate: ◇, ◆) and 1432 cm<sup>-1</sup> (monodentate carbonate, ▲, △) during CO oxidation after 15 h drying in N<sub>2</sub> at 100 °C followed by calcination at 400 °C (open symbols) and after 1000 min reaction and re-calcination at 400 °C (filled symbols).

catalysts, both for non-porous and mesoporous materials, after calcination at 300 °C. They related it to the increasing tendency for Au particle sintering during calcination in the order brookite < anatase < P25 (anatase/rutile)  $\approx$  rutile. In contrast, after reductive treatment at 150 °C both the activities and the Au particle sizes were comparable. Ho and Yeung found the CO oxidation activity of mesoporous Au catalysts to decrease in the order Au/anatase (mesoporous) > Au/P25 (rutile/anatase) > Au/rutile (mesoporous) [13], while in our measurements the activity decreases in the order Au/anatase (mesoporous) > Au/rutile (mesoporous)  $\geq$  Au/P25 (rutile/anatase). Because of the significant differences in the material properties between both studies, a direct comparison is hardly possible. Furthermore, these authors also reported measurable effects of the crystalline phase of TiO<sub>2</sub> on the catalyst deactivation, which increased in the order Au/anatase (mesoporous) > Au/P25 (anatase/rutile) > Au/rutile (mesoporous). Such effects were not observed in our measurements.

In previous measurements of the water gas shift reaction on Au/CeO<sub>2</sub> catalysts it was shown that calcination of the deactivated catalysts at 400 °C in a 10% O<sub>2</sub>/rest N<sub>2</sub> atmosphere (O400 treatment) results in a temporary reactivation of the catalyst, and this was considered as further evidence for the proposal that the deactivation during the reaction is mainly due to the reversible formation of surface species, in particular of surface carbonates, rather than to irreversible Au nanoparticle sintering [60]. Similar experiments were performed also on the mesoporous Au/TiO<sub>2</sub> catalysts (3), (4) and (5), after 1000 min exposure to a reaction atmosphere. Subsequent reaction measurements shown in Fig. 7c and d clearly indicate that calcination (30 min at 400 °C) of the used catalysts (3)–(5) leads to an almost complete re-activation of the catalysts, with the catalysts regaining between 82% and 94% (Fig. 7d, filled symbols, Table 2) of their initial CO oxidation activity. Also the deactivation behavior of the re-activated catalyst (Fig. 7c and d, second run, filled symbols), with an about exponential deactivation and a steady-state activity of 20–30% of the initial activity after 1000 min on stream, closely resembles that of the freshly prepared catalysts (first run, empty symbols). Obviously, also on these catalysts the deactivation is not caused by irreversible Au nanoparticle sintering but rather results from reversible formation of adsorbed reaction side products.

To gain more information on the re-activation process and on the nature of the deactivating species, we followed the formation and removal of adsorbed surface species during reaction and upon re-calcination on the Au/TiO<sub>2</sub>(3) catalyst by DRIFTS measurements. Selected spectra, recorded during CO oxidation on the Au/TiO<sub>2</sub>(3) catalyst after re-calcination, are shown in the left panel in Fig. 8 (Fig. 8a–c) (for background subtraction we used the first spectrum recorded after calcination). The absence of carbonate-, CO<sub>ad</sub>- and CO<sub>2</sub>-related features in the first spectrum, recorded directly after changing from N<sub>2</sub> to the reaction mixture, clearly indicates that the surface species being built up (removed) during the preceding CO oxidation reaction were removed (reappeared) again: All carbonate species were removed. The negative water peak at  $\sim 1617\text{ cm}^{-1}$  indicates that the amount of water on the surface is slightly lower than after the initial calcination of the catalyst. On the other hand, the higher intensity of the isolated OH groups at 3724 and 3675 cm<sup>-1</sup>, which had decreased in intensity during the preceding reaction (oxygen induced conversion from adsorbed hydroxyls to adsorbed water, see above), indicates that these species were built up during the reactivation procedure.

The temporal evolution of the intensities of the different characteristic signals recorded on the Au/TiO<sub>2</sub>(3) catalyst in the first reaction run, after drying and calcination (N15-O400 pre-treatment, filled symbols), and in the second reaction run, after re-calcination (empty symbols), is illustrated in the right panel

(Fig. 8d). The developments of the CO<sub>ad</sub> and CO<sub>2</sub> peak area as well as of the peak heights of the signals at 1617 (water), 1564 (bidentate carbonate) and 1432 cm<sup>-1</sup> (monodentate carbonate) before and after reactivation closely resemble each other, both in absolute intensities and in their trends. These results further support our above proposal that the deactivation of the mesoporous Au/TiO<sub>2</sub> catalysts is dominated by the reversible build-up of adsorbed reaction side products, specifically of surface carbonates, similar to earlier findings for Au/TiO<sub>2</sub> catalysts supported on non-porous P25 [22,40,42]. Thus, the different morphologies of these two materials have little effect on their chemical properties towards carbonate formation, which for both catalysts is facile and results in rapid deactivation. In that sense, the possible stabilization of the Au nanoparticles against sintering in the mesoporous TiO<sub>2</sub> does not affect and improve the catalytic stability, since this is limited by the tendency for surface carbonate formation. These species can be removed by calcination, but because of the rapid re-deactivation of the re-activated catalyst this re-activation procedure is not attractive for practical applications. Any improvement of the catalyst stability will have to start at reducing the tendency for surface carbonate formation. If this problem can be solved, then the higher activity of the mesoporous anatase supported Au/TiO<sub>2</sub> catalysts will make them an attractive alternative to Au/TiO<sub>2</sub> catalysts supported on non-porous commercial materials such as P25.

#### 4. Summary

The influence of the crystalline phase of the support and of the surface area of structurally well-defined mesoporous Au/TiO<sub>2</sub> catalysts with comparable Au loading on the activity and stability/deactivation behavior in the CO oxidation reaction was investigated by kinetic measurements under differential reaction conditions and by *in situ* DRIFTS. The surface area of the mesoporous TiO<sub>2</sub> was varied by the choice of the surfactant, with SDS leading to higher surface areas than Brij56. Its crystalline phase was controlled by variation of the pH during synthesis, leading to anatase at a pH of 2, rutile at pH  $\leq 0$ , and a mixture of anatase and rutile at intermediate pH values. Using the same deposition–precipitation procedure for Au loading and subsequent calcination at 400 °C for all support materials, the resulting Au particles are homogeneously distributed on the support in the different resulting Au/TiO<sub>2</sub> catalysts. For anatase or P25 as support, a mean Au particle size of 3–4 nm are obtained, while for catalysts based on mesoporous rutile the particle size is about 6 nm. On all catalysts, Au is mainly present as metallic Au<sup>0</sup> species after calcination, contributions from ionic Au are below the detection limit.

The use of mesoporous supports can lead to significantly higher CO oxidation activities than obtained for the standard Au/TiO<sub>2</sub> catalyst based on non-porous P25. The highest activity was observed for the mesoporous anatase based catalyst with the lower BET surface area. Going to higher surface area anatase or rutile supports results in activities comparable to that of the P25 based catalyst. All catalysts showed the same exponential decay of the activity with time on stream, with deactivations between 67 and 82% during 1000 min. Apparently, the crystalline phase of the catalyst support has little influence on the inherent (TOF based) activity of the catalysts. It does affect, however, the Au nanoparticle size resulting from the same deposition–precipitation and conditioning procedures. In contrast, the surface area of the mesoporous support plays a sizable role, leading to a decreasing activity of catalysts with higher surface areas, in good agreement with previous reports.

*In situ* DRIFTS as well as TEM measurements indicate that similar to previous observations for P25 based Au/TiO<sub>2</sub> catalysts the mesoporous catalysts deactivate via reversible formation of

reaction inhibiting adsorbed side products, most likely monodentate surface carbonates, rather than by irreversible Au nanoparticle growth. This is supported also by re-activation experiments, which show that calcination of the used catalysts at 400 °C leads to a recovery of the activity, reaching more than 80–90% of the initial activity, and to a similar deactivation behavior as in the initial reaction run on the freshly prepared catalyst. In addition, the deactivation can be reduced by pre-adsorbed water and/or hydroxyl species, probably by lowering the tendency for surface carbonate formation. This lowers also the initial activity, but the steady-state activity is higher than that of a dried catalyst. Similar effects were reported recently also for P25 based Au/TiO<sub>2</sub> catalysts. The close similarity in the deactivation behavior and in the effects of pre-adsorbed water indicates that the chemistry for CO oxidation and for side product formation is similar on the non-porous P25 supported Au/TiO<sub>2</sub> catalyst and on the mesoporous catalysts.

### Acknowledgements

This work was supported by the Deutsche Forschungsgemeinschaft within the Priority Programme (SPP) 1181 'Nanomater' (BE 1201/13-2, HU 1427/1-2 and KA 1295/5-2).

### Appendix A. Supplementary data

Supplementary data associated with this article can be found, in the online version, at [doi:10.1016/j.apcatb.2009.06.016](https://doi.org/10.1016/j.apcatb.2009.06.016).

### References

- [1] M. Haruta, T. Kobayashi, H. Sano, N. Yamada, *Chem. Lett.* (1987) 405.
- [2] M. Haruta, *CATECH* 6 (2002) 102.
- [3] G.C. Bond, C. Louis, D.T. Thompson, *Catalysis by Gold*, World Scientific, 1999.
- [4] M. Haruta, M. Daté, *Appl. Catal. A* 222 (2001) 427.
- [5] Y. Iizuka, T. Tode, T. Takao, K. Yatsu, T. Takeuchi, S. Tsubota, M. Haruta, *J. Catal.* 187 (1999) 50.
- [6] M.M. Schubert, S. Hackenberg, A.C. van Veen, M. Muhler, V. Plzak, R.J. Behm, *J. Catal.* 197 (2001) 113.
- [7] S.H. Overbury, L. Ortiz-Soto, H. Zhu, B. Lee, M.D. Amiridis, S. Dai, *Catal. Lett.* 95 (2004) 99.
- [8] J.J. Pietron, R.M. Stroud, D.R. Rolison, *Nano Lett.* 2 (2002) 545.
- [9] J.-H. Liu, Y.-S. Chi, H.-P. Lin, C.-Y. Mou, B.-Z. Wan, *Catal. Today* 93–95 (2004) 141.
- [10] C.-W. Chiang, A. Wang, B.-Z. Wan, C.-Y. Mou, *J. Phys. Chem. B* 109 (2005) 18042.
- [11] C.-W. Chiang, A. Wang, C.-Y. Mou, *Catal. Today* 117 (2007) 220.
- [12] Y. Denkwitz, J. Geserick, U. Hörmann, V. Plzak, U. Kaiser, N. Hüsing, R.J. Behm, *Catal. Lett.* 119 (2007) 199.
- [13] K.Y. Ho, K.L. Yeung, *Gold Bull.* 40 (2007) 15.
- [14] D. Wang, Z.D.S. Ma, J. Liu, Z. Nie, M.H. Engelhard, Q. Huo, C. Wang, R. Kou, *J. Phys. Chem. C* 112 (2008) 13499.
- [15] Y. Zhu, W. Li, Y. Zhou, X. Lu, X. Feng, Z. Yang, *Catal. Lett.* 127 (2009) 406.
- [16] S.D. Lin, M.A. Bollinger, M.A. Vannice, *Catal. Lett.* 17 (1993) 245.
- [17] N. Perkas, Z. Zhing, J. Grinblat, A. Gedanken, *Catal. Lett.* 120 (2008) 19.
- [18] G.C. Bond, D.T. Thompson, *Catal. Rev. Sci. Eng.* 41 (1999) 319.
- [19] M. Haruta, *Catal. Surv. Jap.* 1 (1997) 61.
- [20] F. Boccuzzi, A. Chiorino, *J. Phys. Chem. B* 104 (2000) 5414.
- [21] G.C. Bond, D.T. Thompson, *Gold Bull.* 33 (2000) 41.
- [22] B. Schumacher, Y. Denkwitz, V. Plzak, M. Kinne, R.J. Behm, *J. Catal.* 224 (2004) 449.
- [23] B. Schumacher, V. Plzak, M. Kinne, R.J. Behm, *Catal. Lett.* 89 (2003) 109.
- [24] F. Moreau, G.C. Bond, *Appl. Catal. A* 302 (2006) 110.
- [25] V. Schwartz, D.R. Mullins, W. Yan, B. Chen, S. Dai, S.H. Overbury, *J. Phys. Chem. B* 108 (2004) 15782.
- [26] W. Yan, B. Chen, S.M. Mahurin, V. Schwartz, D.R. Mullins, A.R. Lupini, S.J. Pennycook, S. Dai, S.H. Overbury, *J. Phys. Chem. B* 109 (2005) 10676.
- [27] M. Comotti, C. Weidenthaler, W.-C. Li, F. Schüth, *Top. Catal.* 44 (2007) 275.
- [28] J. Geserick, N. Hüsing, R. Rosmanith, K. Landfester, C.K. Weiss, Y. Denkwitz, R.J. Behm, U. Hörmann, U. Kaiser, *Mater. Res. Soc. Symp. Proc.* 1007, Materials Research Society, Boston, 2008, p. S04-13.
- [29] Y. Denkwitz, B. Schumacher, G. Kucerova, R.J. Behm, submitted for publication.
- [30] Y. Xia, J. Xuchuan, T. Herricks, *Adv. Mater.* 15 (2003) 1205.
- [31] V. Plzak, J. Garche, R.J. Behm, *Eur. Fuel Cell News* 10 (2003) 8.
- [32] E.P. Barrett, L.G. Joyner, P.P. Halenda, *J. Am. Chem. Soc.* 73 (1951) 373.
- [33] J.F. Moulder, W.F. Stickle, P.E. Sobol, K.D. Bomben, *Handbook of X-ray Photoelectron Spectroscopy*, Perkin Elmer Corp., Eden Prairie/USA, 1992.
- [34] M.J. Kahlich, H.A. Gasteiger, R.J. Behm, *J. Catal.* 171 (1997) 93.
- [35] P.B. Weisz, *Chem. Eng. Prog. Symp. Ser.* 55 (1992) 29.
- [36] I.M. Hamadeh, P.R. Griffiths, *Appl. Spec.* 41 (1987) 682.
- [37] F. Meunier, A. Goguet, R. Burch, D. Thompsett, *J. Catal.* 252 (2007) 18.
- [38] W. Huang, X. Tang, Y. Wang, Y. Kolytyn, A. Gedanken, *Chem. Commun.* (2000) 1415.
- [39] R. Mueller, H.K. Kammler, K. Wegner, S.E. Pratsinis, *Langmuir* 19 (2003) 160.
- [40] Y. Denkwitz, Z. Zhao, U. Hörmann, U. Kaiser, V. Plzak, R.J. Behm, *J. Catal.* 251 (2007) 363.
- [41] U. Hörmann, J. Geserick, S. Selve, A. Kaiser, N. Hüsing, in: S. Richter, A. Schwedt (Eds.), *Proceedings of the EMC 2008—Materials Science*, vol. 2, Springer, Berlin, 2009, pp. 219–220.
- [42] R. Zanella, S. Giorgio, C.-H. Shin, C.R. Henry, C. Louis, *J. Catal.* 222 (2004) 357.
- [43] P. Konova, A. Naydenov, C. Venkov, D. Mehandjiev, D. Andreeva, T. Tabakova, *J. Mol. Catal. A* 213 (2004) 235.
- [44] B. Schumacher, V. Plzak, J. Cai, R.J. Behm, *Catal. Lett.* 101 (2004) 215.
- [45] M.I. Zaki, H. Knözinger, *Mater. Chem. Phys.* 17 (1987) 201.
- [46] K.S. Kim, M.A. Barteau, *Langmuir* 4 (1988) 945.
- [47] K.S. Finnie, D.J. Cassidy, J.R. Bartlett, J.L. Woolfrey, *Langmuir* 17 (2001) 816.
- [48] F. Boccuzzi, A. Chiorino, S. Tsubota, M. Haruta, *J. Phys. Chem.* 100 (1996) 3625.
- [49] M.A. Bollinger, M.A. Vannice, *Appl. Catal. B* 8 (1996) 417.
- [50] J.-D. Grunwaldt, M. Maciejewski, O.S. Becker, P. Fabrizioli, A. Baiker, *J. Catal.* 186 (1999) 458.
- [51] H. Klimev, K. Fajerwerk, K. Chakarova, L. Delannoy, C. Louis, K. Hadjiivanov, *J. Mater. Sci.* 42 (2007) 3299.
- [52] N. Weiher, A.M. Beesley, N. Tsapatsaris, C. Louis, L. Delannoy, J.A. van Bokhoven, S.L.M. Schröder, *AIP Conf. Proceed.* 882 (2007) 600.
- [53] A.A. Davydov, *Infrared Spectroscopy of Adsorbed Species on the Surface of Transition Metal Oxides*, John Wiley & Sons Ltd., Chichester, UK, 1984.
- [54] M. Daté, M. Haruta, *J. Catal.* 201 (2001) 221.
- [55] B. Schumacher, Ph.D. thesis, Ulm University, 2005.
- [56] M.A. Henderson, *J. Phys. Chem. B* 101 (1997) 221.
- [57] E.D. Park, J.S. Lee, *J. Catal.* 186 (1999) 1.
- [58] J.T. Calla, R.J. Davis, *J. Catal.* 241 (2006) 407.
- [59] M.A. Debeila, R.P.K. Wells, J.A. Anderson, *J. Catal.* 239 (2006) 162.
- [60] A. Karpenko, R. Leppelt, J. Cai, V. Plzak, A. Chuvilin, U. Kaiser, R.J. Behm, *J. Catal.* 250 (2006) 139.